VPS35 deficiency in the embryonic cortex leads to prenatal cell loss and abnormal development of axonal connectivity

Micaela Roque, Diego Alves Rodrigues de Souza, Martha M Rangel-Sosa, Mike Altounian, Mélanie Hocine, Jean-Christophe Deloulme, Emmanuel L Barbier, Fanny Mann, Sophie Chauvet

Molecular and Cellular Neuroscience 120 (2022) 103726

Contents lists available at ScienceDirect

Molecular and Cellular Neuroscience

journal homepage: www.elsevier.com/locate/ymcne

VPS35 deficiency in the embryonic cortex leads to prenatal cell loss and abnormal development of axonal connectivity

Micaela Roque [a], Diego Alves Rodrigues de Souza [b], Martha M. Rangel-Sosa [a], Mike Altounian [a], Mélanie Hocine [a], Jean-Christophe Deloulme [b], Emmanuel L. Barbier [b], Fanny Mann [a,1], Sophie Chauvet [a,*,1]

[a] Aix Marseille Univ, CNRS, IBDM, Marseille, France
[b] Univ. Grenoble Alpes, Inserm, U1216, Grenoble Institut Neurosciences, 38000 Grenoble, France

ARTICLE INFO

Keywords:
VPS35
Retromer
Axon guidance
Neurogenesis
Cell death
DTI
3D imaging
Mice

ABSTRACT

VPS35 is a core component of the retromer complex involved in familial forms of neurodegenerative diseases such as Parkinson's and Alzheimer's disease. In mice, VPS35 is expressed during early brain development. However, previous studies have reported that VPS35 activity is largely dispensable for normal neuronal development and initial elaboration of axonal projections. Here, we evaluated the role of VPS35 in the mouse embryonic brain using two Cre-driver lines that remove *Vps35* from the cortex at different prenatal stages. We found that *Vps35* mutant mice displayed microcephaly and decreased cortical thickness from the embryonic stages to adulthood. VPS35 also regulates cortical development by affecting a subpopulation of neural progenitor cells and the survival of postmitotic neurons. In addition, we showed that a lack of VPS35 leads to hypoplasia and misrouting of several axonal projections, including the anterior commissure and fornix. Furthermore, VPS35 deficiency impairs the non-autonomous development of thalamocortical axons (TCAs), which show severe disruption of innervation and terminal arborization in the cortex. Together, these data demonstrate that VPS35 plays a greater role in embryonic development of the mammalian brain than it was previously thought.

1. Introduction

Advances in the study of brain development have elucidated the mechanisms that guide neurogenesis and neuronal connection patterning. Alterations in these processes caused by genetic or environmental perturbations are linked to the pathogenesis of various neurodevelopmental disorders. Moreover, accumulating evidence suggests that early brain development is a critical period for the development of late-onset neurodegenerative disorders. Indeed, recent data have demonstrated aberrant neural development in human foetuses carrying the Huntington's disease mutation (Barnat et al., 2020), suggesting that events initiated before birth might enhance susceptibility to degenerative diseases in later life. Thus, evaluating the function of genes associated with age-related neurodegenerative pathologies during the early stages of brain development is of crucial importance.

The VPS35 (vacuolar protein sorting-associated protein 35) gene is involved in several neurodegenerative pathologies. A pathogenic mutation in VPS35 has been identified in families with autosomal dominant forms of Parkinson's disease (PD) (Vilariño-Güell et al., 2011; Zimprich et al., 2011). In addition, mice hemizygous for *Vps35* or with selective deletion of *Vps35* in dopaminergic neurons exhibit age-dependent loss of dopaminergic neurons and accumulation of α-synuclein protein, two pathological hallmarks of the disease (Tang et al., 2015). Moreover, downregulation of VPS35 expression has been reported in brain regions affected by Alzheimer's disease (AD) (Small et al., 2005). More recently, VPS35 was also found to be reduced in the brains of patients with Down's syndrome (DS), indicating its possible involvement in the development of AD-like pathology in such patients (Curtis et al., 2020).

These implications are explained by the fact that VPS35 is a core component of the retromer complex, a heteropentameric protein complex found in all eukaryotic cells. The best-known activity of the retromer is the retrieval and recycling of protein cargos from the endosome to the trans-Golgi network or the plasma membrane (Seaman, 2012). In

* Corresponding author.
E-mail address: sophie.chauvet@univ-amu.fr (S. Chauvet).
[1] equal contribution.

https://doi.org/10.1016/j.mcn.2022.103726
Received 31 March 2021; Received in revised form 25 March 2022; Accepted 27 March 2022
Available online 31 March 2022

addition, the retromer is associated with the autophagy-lysosomal degradation pathway and mitochondrial functions (Chen et al., 2019). Thus, the retromer is a central actor in the maintenance of cellular proteostasis, and its impairment might trigger the accumulation of toxic proteins and damaged organelles, potentially causing neuronal cell death (Brodin and Shupliakov, 2018).

During development, *Vps35* is highly expressed in the pyramidal neurons of the mouse cortex (Wang et al., 2012; Wen et al., 2011). Selective deletion of *Vps35* in newly born pyramidal (post-mitotic) neurons (by Nex/Neurod6-Cre) leads to altered terminal differentiation of cortical axons and dendrites, together with early onset of degenerative-like pathology (Tang et al., 2020). Specifically, $Vps35^{Nex}$ cKO mice show increased neuronal apoptosis and progressive cortical atrophy beginning two weeks after birth (around postnatal day (P) 14). These data support the idea that *Vps35* deficiency is a common pathological mechanism of neurodegenerative disorders and could represent a risk factor for frontotemporal dementia, in which pyramidal neurons are the most affected cells (Tang et al., 2020).

Although *Vps35* is expressed in the developing mouse cortex, there is no evidence for its role in embryonic brain development. Moreover, its role during corticogenesis remains unknown. However, in vivo studies in invertebrate species have reported important functions of *Vps35* in several developmental processes. Notably, *Vps35* regulates cell polarity in the *Drosophila* embryo and wing discs by recycling various cargos such as Crumbs and planar polarity proteins (Pocha et al., 2011; Strutt et al., 2019; Zhou et al., 2011). In the *Drosophila* brain, *Vps35* prevents the aberrant dedifferentiation of neural progenitors back into neuroblasts by trafficking Notch (Li et al., 2018), while in *C. elegans, Vps35* establishes the anteroposterior polarity of mechanosensory neurons by regulating Wnt signaling (Prasad and Clark, 2006). These data suggest that *Vps35* could regulate neural progenitor cell proliferation and differentiation in the mammalian brain. A recent study used Emx1-Cre mice to delete the *Vps35* gene in progenitor cells of the dorsal telencephalon (Wu et al., 2020). The resulting $Vps35^{Emx1}$ conditional knock-out (cKO) mice showed ventriculomegaly and severe cortical thickness decrease starting at P7, an age when brain development appears normal in $Vps35^{Nex}$ cKO mutants. This difference is partly due to an alteration in the differentiation and survival of ependymal cells lining the cerebral ventricles, which are derived from radial glia progenitors, leading to the development of hydrocephalus (Wu et al., 2020). However, it remains to be determined whether the marked thinning of the cerebral cortex in $Vps35^{Emx1}$ cKO mice indicates additional functions of *Vps35* in neural *progenitor* cells.

Herein, we performed a detailed analysis of cortical development in $Vps35^{Emx1}$ cKO mice and compared it to that in $Vps35^{Nex}$ cKO mice. Consequently, we demonstrated an early function of *Vps35* in a subpopulation of progenitor cells in $Vps35^{Emx1}$ cKO mice. In addition, contrary to the established idea of age-dependent neuronal loss, we also found that *Vsp35* deficiency affects neuronal survival and cortex size before birth, not only in $Vps35^{Emx1}$ cKO mice, but also in $Vps35^{Nex}$ cKO mice. This fining has not been reported to date. Finally, this analysis reported an important function of VPS35 in controlling axon guidance and targeting in both $Vps35^{Emx1}$ cKO and $Vps35^{Nex}$ cKO mutants. We, therefore, found that the inability of thalamic axons to innervate the *Vps35* deficient cortex leads to non-autonomous neuronal cell death in the thalamus.

These data provide evidence that embryonic VPS35 is necessary for brain development and connectivity, thereby opening the possibility that VPS35-linked neurodegenerative disorders are associated with defects already present in the early stages of development.

2. Results

2.1. Autonomous and non-autonomous effect of Vps35 deletion on brain structure and connectivity

In this study, we employed a conditional knockout approach by breeding *Vps35* floxed mouse line ($Vps35^{lox/lox}$) with the *Emx1-Cre* transgenic line that resulted in the ablation of *Vps35* in progenitor cells and their progeny in the cortex and hippocampus, beginning around embryonic day (E) 9.5 (Guo et al., 2000). RT-qPCR analysis confirmed that *Vps35* mRNA expression was significantly reduced in tissue expressing the cre-recombinase (supplemental Fig. 1A,B). Mutant embryos exhibit grossly normal appearance and body weight (supplemental Fig. 1E), however, after birth, $Vps35^{Emx1}$ cKOs display impaired growth rate compared to wild-type (WT) and heterozygous littermates, as evidenced by reduced body size and weight at postnatal day (P) 21 (supplemental Fig. 1G,H). These observations were similar to $Vps35^{Nex}$ mice in which *Vps35* is selectively deleted in newly born pyramidal neurons (supplemental Fig. 1C,D,F,I,J). The high lethality of $Vps35^{Emx1}$ cKO mice has been previously reported during weaning (P20-P25) (Wu et al., 2020). However, we found that in refined housing conditions, with access to hydrated food on the cage floor, viability was restored, and animals could reach adulthood (data not shown). Therefore, we used ex vivo magnetic resonance imaging (MRI) to inspect the brain anatomy of adult (10 weeks old) $Vps35^{Emx1}$ cKO mice. Brain structures were segmented, and their volumes were quantified using three-dimensional (3D) reconstruction of MRI images. Compared to WT, $Vps35^{Emx1}$ cKO animals showed severe microcephaly, which was associated with cortical and hippocampal atrophy (Fig. 1A-D) as well as ventriculomegaly (Fig. 1G). In contrast, the brain structures not targeted by *Emx1-Cre*, such as the cerebellum, remained unaffected (Fig. 1A,E). A notable exception, however, was the thalamus, which has extensive connections with the entire cerebral cortex, and its volume was reduced by approximately 56% in $Vps35^{Emx1}$ mutants compared to controls (Fig. 1A,F).

Diffusion tensor imaging (DTI) was used to gain information about the connectivity of the $Vps35^{Emx1}$ brains. The streamline fibre tracts were reconstructed for the major projection pathways into and out of the cortex and hippocampus (Fig. 1H). $Vps35^{Emx1}$ cKO showed a strong reduction in inter-hemispheric projections, including the corpus callosum, anterior commissure, and hippocampal commissure (Fig. 1I-K). Analysis also reported a significant reduction in the fornix, the main efferent pathway of the hippocampal formation, and of the internal capsule, that carries both afferent and efferent fibres of the cerebral cortex (Fig. 1L,M). In contrast, no significant differences were found in the number of streamlines passing through the fasciculus retroflexus, which originates from habenular neurons not targeted by *Emx1-Cre* (Fig. 1N).

Thus, the selective suppression of *Vps35* in progenitor cells and postmitotic neurons of the dorsal telencephalon leads to a reduction in the volume of the cerebral cortex and its connectivity in adults. It also resulted in non-autonomous atrophy of the thalamus.

2.2. Prenatal onset of cortical atrophy in conditional VPS35 mutants

To determine whether the reduced cortex in $Vps35^{Emx1}$ cKOs results from age-related neuronal loss, hydrocephalus, and/or earlier developmental defects, we measured changes in cortical thickness during embryonic and early postnatal life (from E14.5 to P21) (Fig. 2A-C). At E14.5 there was no difference in cortical thickness between WT and

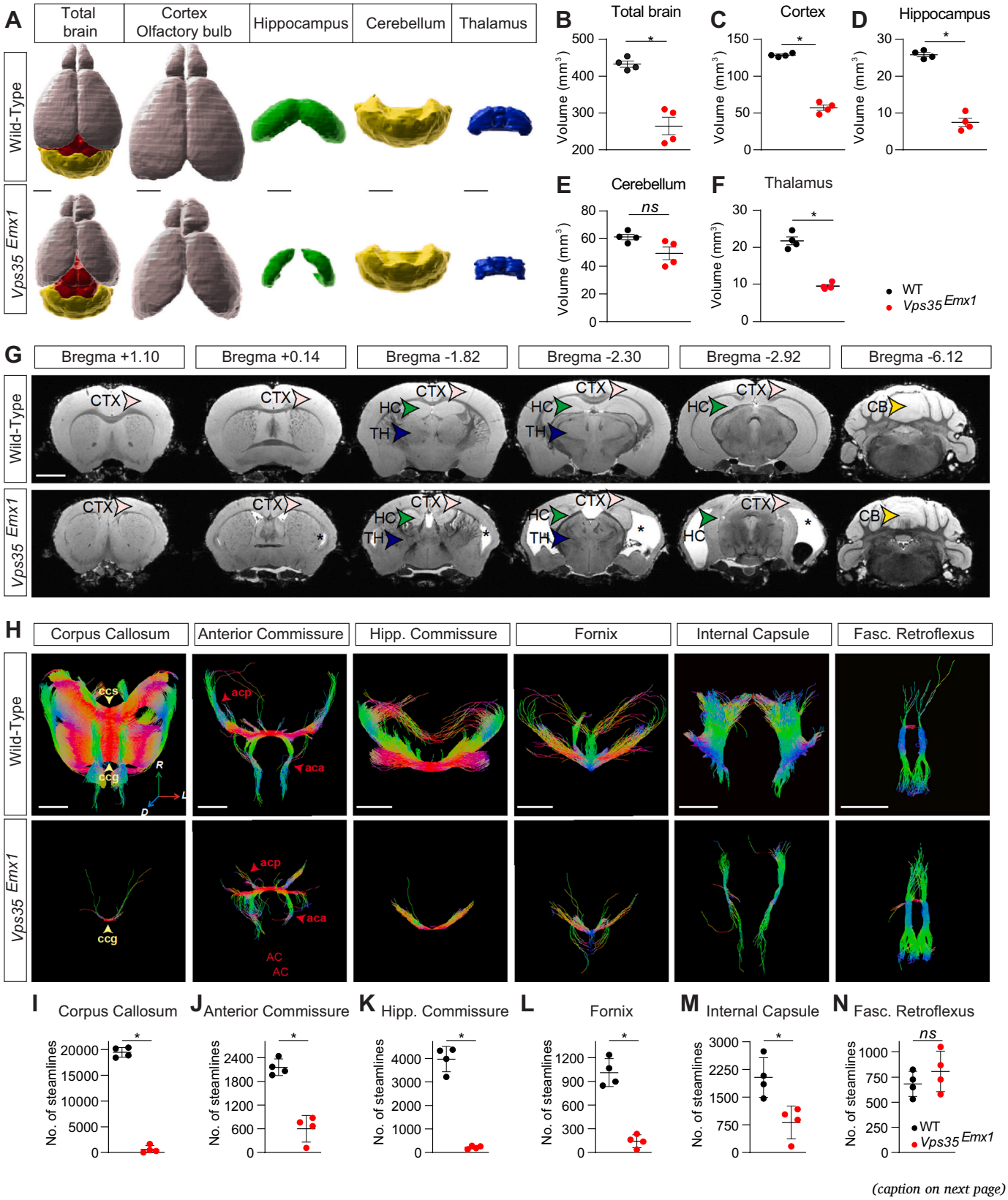

(caption on next page)

Fig. 1. Autonomous and non-autonomous effect of embryonic *Vps35* deletion on brain structure and connectivity. Selective suppression of *Vps35* in progenitor cells of the dorsal telencephalon leads to a reduction in the volume of the cerebral cortex and its connectivity in adults, as well as non-autonomous atrophy of the thalamus.

A. 3D reconstruction of brain structures upon ex vivo MRI of 10 weeks old mice showed that $Vps35^{Emx1}$ cKO animals present severe microcephaly when compared to the wild-type (WT) mice. This is associated with cortical (light grey) and hippocampal (green) atrophy. Hindbrain is depicted in red, cerebellum in yellow, and thalamus in blue.

B-F. Quantification of the volumes from the 3D reconstructions presented in A. Data represent the mean ± S.D. WT: $n = 4$ mice; $Vps35^{Emx1}$ cKO: n = 4 mice. Mann-Whitney tests.

B. Total brain volume average ± S.D. WT, 432.6 ± 16.65 mm^3 versus $Vps35^{Emx1}$ cKO, 264.7 ± 47.55 mm^3 ($^*P = 0.0286$).

C. Cortex volume average ± S.D. WT, 128.5 ± 2.193 mm^3 versus $Vps35^{Emx1}$ cKO, 57.11 ± 7.331 mm^3 ($^*P = 0.0286$).

D. Hippocampus volume average ± S.D. WT, 25.83 ± 1.098 mm^3 versus $Vps35^{Emx1}$ cKO, 7.468 ± 2.312 mm^3 (*P = 0.0286).

E. Cerebellum volume average ± S.D.: WT, 61.26 ± 3.905 mm^3 versus $Vps35^{Emx1}$ cKO, 49.39 ± 9.173 mm^3 (n.s. $P = 0.0571$).

F. Thalamus volume average ± S.D.: WT, 18.119 ± 1.812 mm^3 versus $Vps35^{Emx1}$ cKO, 7.950 ± 0.7276 mm^3 (*P = 0.0286).

G. Ex vivo MRI sections at the indicated distances from the bregma of WT and $Vps35^{Emx1}$ cKO adult brains. The different sections reveal a reduction in cortex width from the anterior most to the posterior most regions (pink arrowheads), as well as a reduction in the hippocampus (green arrowheads). In contrast, the cerebellum (yellow arrowheads) was not significantly affected. A notable exception is the thalamus (blue arrowheads), which is also reduced. In addition, it is possible to observe ventriculomegaly (asterisks) in the mutant animals.

H. DTI used to gain information on the connectivity of WT and $Vps35^{Emx1}$ cKO brains. Streamline fibre tracts were reconstructed for the major projection pathways into and out of the cortex and hippocampus, as indicated in the figure.

I-N. Graphs plotting the number of streamline fibres for the indicated tracts in WT and $Vps35^{Emx1}$ cKO animals. The $Vps35^{Emx1}$ cKO brains show a strong reduction in inter-hemispheric projections. Data represent the mean ± S.D. WT: $n = 4$ mice; $Vps35^{Emx1}$ cKO: n = 4 mice. Mann-Whitney tests.

I. Strong reduction of the corpus callosum (cc, 97%) [number of streamlines ± S.D. WT, 19464 ± 956.7 versus $Vps35^{Emx1}$ cKO, 616.3 ± 732.3 ($^*P = 0.0286$)].

J. Reduction of the anterior commissure (ac, 32%) [number of streamlines ± S.D. WT, 2158 ± 209.1 versus $Vps35^{Emx1}$ cKO, 604.0 ± 338.5 ($^*P = 0.0286$)].

K. Strong reduction of the hippocampal commissure (hc, 95%) [number of streamlines ± S.D. WT, 3971.0 ± 535.9 versus $Vps35^{Emx1}$ cKO, 216.3 ± 66.56 ($^*P = 0.0286$)].

L. Strong reduction of the fornix (f, 86%) [number of streamlines ± S.D. WT, 1011 ± 177.2 versus $Vps35^{Emx1}$ cKO, 142.8 ± 82.26 (*P = 0.0286)].

M. Reduction of the internal capsule (ic, 60%) [number of streamlines ± S.D.: WT, 2035 ± 535.0 versus $Vps35^{Emx1}$ cKO, 817.0 ± 447.6 (*P = 0.0286)].

N. No significant differences were found in the number of streamlines passing through the fasciculus retroflexus (fr) [number of streamlines ± S.D. WT, 682.5 ± 124.3 versus $Vps35^{Emx1}$ cKO, 805.8 ± 201.1 (n.s. $P = 0.4857$)].

CTX, cortex; HC, hippocampus; TH, thalamus; CB, cerebellum; ccs, corpus callosum splenium; ccg, corpus callosum genu; aac, anterior commissure; pac, posterior anterior commissure. Scale bars: 2 mm. (For interpretation of the references to colour in this figure legend, the reader is referred to the web version of this article.)

$Vps35^{Emx1}$ cKO embryos. However, from E16.5, the mutant cortex was significantly thinner than normal (Fig. 2A-C). To confirm these data, we used whole brain light-sheet imaging to quantify brain volumes after 3D reconstruction of the autofluorescence signal. We found a significant reduction in total brain volume (−8.4 ± 2.5 mm^3) in E18.5 $Vps35^{Emx1}$ cKOs, which was largely due to a decrease in cortical volume (−5.1 ± 0.87 mm^3) and ventricles (−0.02 ± 0.01 mm^3) (Fig. 2D-F). Consistently, no difference was observed when measuring 'total brain volume minus cortex volume' or striatal volume (Fig. 2G,H). These data indicate an early effect of *Vps35* deficiency on cortical development that occurs before hydrocephalus is established (~P7) in $Vps35^{Emx1}$ cKO mice (Fig. S2A, Wu et al., 2020). Surprisingly, we also observed a prenatal onset at E18.5, in the reduction of cortical thickness in $Vps35^{Nex}$ cKO mice, although the decrease was less pronounced than in $Vps35^{Emx1}$ cKO mice (supplemental Fig. 2B-J). These results are in contrast to previous reports wherein post-natal age-related thinning of the cortex was only seen in mutants from P7 onwards (Tang et al., 2020).

We then examined the laminar cytoarchitecture of the *Vps35* mutant cortices. First, we used in utero electroporation to deliver Cre recombinase plasmids in cortical progenitors of $Vps35^{lox/lox}$ embryos at E14.5. When analyzed at E17.5, before cortical defects appeared in both *Vps35* cKO embryos, migrating Cre-electroporated neurons showed a normal distribution throughout the developing cortex, including the ventricular zone, the intermediate zone, and the cortical plate (supplemental Fig. 3A-C). In addition, we labelled cohorts of neurons with EdU at E14.5 and examined the number and localisation of labelled neurons at P3 (supplemental Fig. 3D). In both WT and $Vps35^{Emx1}$ cKO cortices, neuronal migration and proliferation were not affected (supplemental Fig. 3D,E), in line with previously reported results (Tang et al., 2020). Despite the overall reduction in cortex size, a normal distribution of the laminar markers, Cux1 (layers 2–4), Rorβ (layer 4), Er81 (layer 5), Ctip2 (layer 5b), and Tbr1 (layer 6) was also observed in the mature cortex at P21 (Fig. 2I-R). Moreover, correct lamination was observed in the reduced brains of $Vps35^{Nex}$ mice (supplemental Fig. 3F-J).

These data indicate an early role of *Vps35* in neurodevelopment, which leads to prenatal atrophy of the cortex in both $Vps35^{Emx1}$ and $Vps35^{Nex}$, without cortical lamination defects.

2.3. Reduced basal progenitor population in the $Vps35^{Emx1}$ cortex

We hypothesised that the greater reduction in cortical thickness observed in $Vps35^{Emx1}$ embryos compared to $Vps35^{Nex}$ cKO mice could be due to defects in neural progenitors. Consequently, we performed immunostaining with the proliferation marker Ki67 (expressed in the entire proliferative zone by all cells going through division) and pHH3 (phospho-histone H3, a marker for mitosis), which more specifically labels cells undergoing mitosis on the apical (ventricular) and basal (parenchymal) sides of the ventricular/subventricular zone (Florio and Huttner, 2014). At mid-corticogenesis (E14.5), we found a marked decrease in the number of $Ki67^+$ cells in the cortex of $Vps35^{Emx1}$ cKO mutants compared to controls (Fig. 3A,B). We also noticed a 52.5% reduction in basal $pHH3^+$ cells, while the number of apical $pHH3^+$ cells remained unchanged (Fig. 3C-E). This finding was further supported by staining basal progenitors with Tbr2 (Arnold et al., 2008), which revealed a 28% reduction in labelled cells in $Vps35^{Emx1}$ cKO (Fig. 3F,G). However, no significant difference in the number of $Pax6^+$ apical progenitors (Gotz et al., 1998) was observed (Fig. 3H,I). Finally, as expected, analysis of $Vps35^{Nex}$ cKO mutants did not reveal any defects in progenitor cells (supplemental Fig. 4). Together, these results demonstrate a specific alteration of the basal progenitor population in the embryonic $Vps35^{Emx1}$ cKO cortex.

2.4. Developmental neuronal loss in $Vps35^{Emx1}$ and $Vps35^{Nex}$ mutants

Defects in progenitor cells could lead to the generation of fewer neurons in the brain of $Vps35^{Emx1}$ cKOs. Additional mechanisms such as the early loss of pyramidal neurons, might also contribute to cortical atrophy, particularly in $Vps35^{Nex}$ mutants. Indeed, immunostaining of brain sections with an antibody against active caspase-3 showed an increase in apoptotic cell death in the neocortex at E14.5, for both $Vps35^{Emx1}$ and $Vps35^{Nex}$ mutant genotypes (Fig. 4A-C and supplemental Fig.A-C). Interestingly, caspase-3^+ cells are predominantly located in the

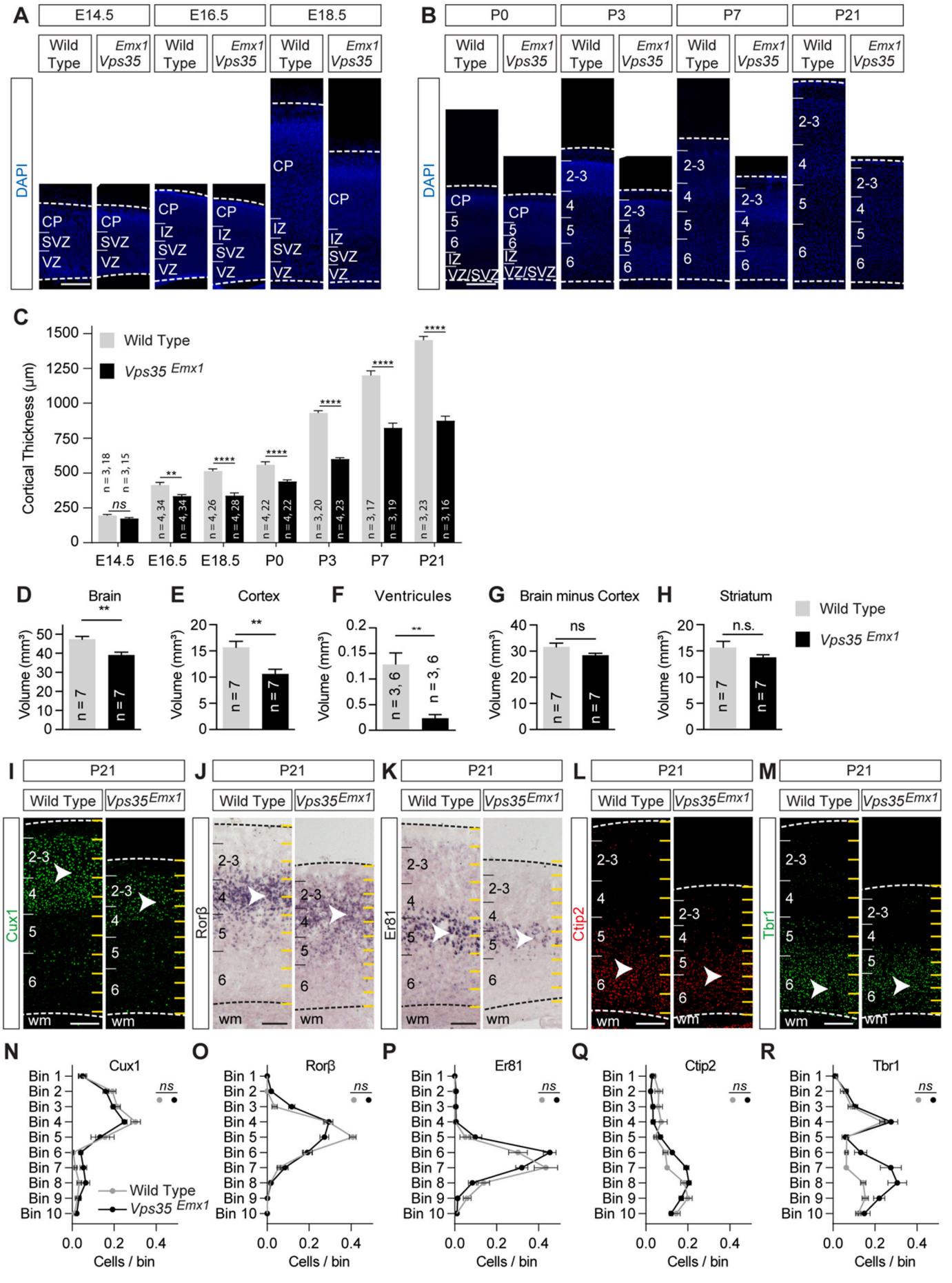

(caption on next page)

Fig. 2. Prenatal onset of cortical atrophy in conditional *VPS35*^{Emx1} mutants. The early role of *Vps35* in neurodevelopment leads to prenatal atrophy of the cortex in *Vps35*^{Emx1} cKO, without cortical lamination defects.
A-B. DAPI-staining of embryonic and postnatal cortical slices of WT and *Vps35*^{Emx1} cKO animals at the indicated ages. Cortical areas and layers are indicated.
C. Graph showing the cortical thickness measured by DAPI staining on cortical sections from A and B. At E14.5 there is no difference in cortical thickness between WT and *Vps35*^{Emx1} cKO embryos [cortical thickness ± S.E.M. E14.5 WT, 194.9 ± 7.34 μm versus cKO, 172.8 ± 9.217 μm (n.s. $P = 0.0672$)]; while from E16.5 onwards, the mutant cortex is significantly smaller than normal [cortical thickness ± S.E.M E16.5 WT, 413.7 ± 18.7 μm versus cKO, 333.7 ± 12.6 μm (**$P = 0.000701$); E18.5 WT, 513.3 ± 16.4 μm versus cKO, 338.2 ± 18.2 μm (****$P < 0.000001$); P0 WT, 558.7 ± 22.4 μm versus cKO, 439.6 ± 11.3 μm (****$P < 0.0001$); P3 WT, 930.6 ± 16.8 μm versus cKO, 599.4 ± 10.4 μm (****P < 0.0001); P7 WT, 1199 ± 33.5 μm versus cKO, 823.1 ± 35 μm (****P < 0.0001); P21 WT, 1452 ± 26.5 μm versus cKO, 874.5 ± 32.9 μm (****P < 0.0001)]. Mann-Whitney tests.
D-H. Graph showing volumes of total brain (D), cortex (E), ventricules (F), brain volume minus cortex (G) or striatum (H), of WT and *Vps35*^{Emx1} cKO animals at E.18.5. Data represent the mean ± SEM (**$P = 0.0023$ (D), **$P = 0.0082$ (E), **$P = 0.0022$ (F), n.s. $P = 0.097$ (G), n.s. $P = 0.0781$ (H)). Mann-Whitney tests.
I - M. Immunostaining for the laminar markers Cux1 (I), Ctip2 (J), and Tbr1 (K) and in situ hybridisation for the laminar markers Rorβ (L) and Er81 (M) in the somatosensory cortex of adult WT and *Vps35*^{Emx1} cKO mice. Cortical areas and layers are indicated.
N – R. Graphs showing a normal distribution of the laminar markers from I-M between WT and *Vps35*^{Emx1} cKO mice (n.s. $P > 0.05$). Ten equal-sized bins were drawn over each image to quantify the distribution of the different markers. Data represent the mean ± SEM. Mann-Whitney tests.
CP, cortical plate; SVZ, subventricular zone; VZ, ventricular zone; IZ, intermediate zone; wm, white matter. n = x,y where x indicates the number of mice and y the number of sections analyzed for each condition (C), n = x where x indicates the number of mice (D,E,G,H), n = x,y where x indicates the number of mice and y the number of ventricles analyzed for each condition (F). Scale bars: 100 μm (A) and 200 μm (B, I-M).

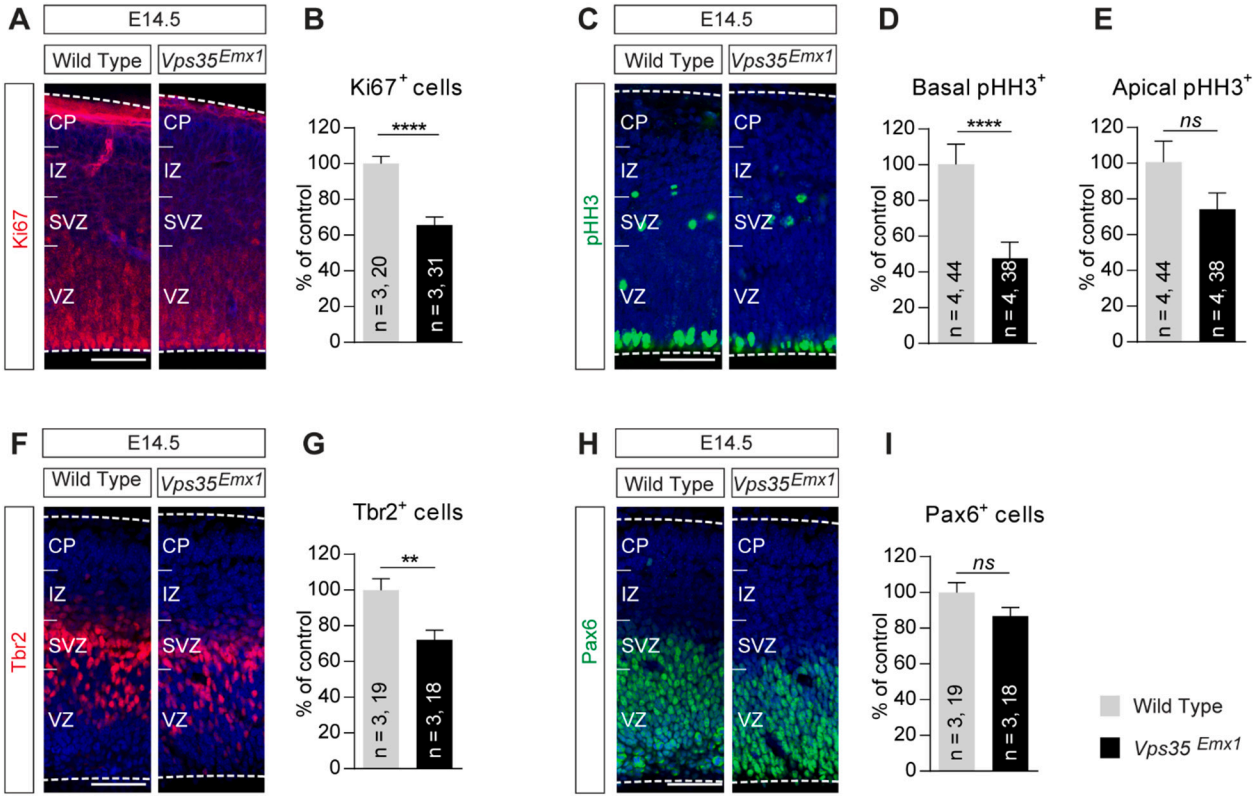

Fig. 3. Specific reduction of the basal progenitor pool in the embryonic *Vps35*^{Emx1} cKO cortex.
A,C,F,H. Immunostaining of WT and *Vps35*^{Emx1} cKO animals at E14.5 for the indicated markers. Cortical areas and layers are indicated.
B,D,E,G,I. Quantification graphs for the respective immunostainings. Data represent the mean ± SEM. Mann-Whitney tests.
A. Immunostaining for the proliferation marker Ki67.
B. A 34% decrease in the number of Ki67$^+$ cells in the neocortex of *Vps35*^{Emx1} cKO mutants compared to controls (****$P < 0.0001$).
C. Immunostaining for the mitotic marker pHH3.
D. A 52.5% specific reduction in basal pHH3$^+$ cells in the neocortex of *Vps35*^{Emx1} cKO mutants compared to controls (****P < 0.0001).
E. The number of apical pHH3$^+$ cells remain unchanged between *Vps35*^{Emx1} cKO mutants and controls (n.s. $P = 0.1627$).
F. Immunostaining of basal progenitors with Tbr2.
G. A 28% reduction in the number of Tbr2$^+$ basal progenitor cells in the neocortex of *Vps35*^{Emx1} cKO mutants compared to controls (**$P = 0.0048$).
H. Immunostaining of apical progenitors with Pax6.
I. No significant difference in the number of Pax6$^+$ apical progenitors between *Vps35*^{Emx1} cKO mutants and controls (n.s. $P = 0.0796$).
CP, cortical plate; IZ, intermediate zone; SVZ, subventricular zone; VZ, ventricular zone. n = x,y where x indicates the number of mice and y the number of sections analyzed for each condition. Scale bars: 50 μm.

proliferating area (ventricular/subventricular zone) of the *Vps35*^{Emx1} cortex, while they are distributed in the postmitotic region (cortical plate) of *Vps35*^{Nex} brains. Increased cell death in the cortical plate was also visible at E18.5 and P3, stages at which neuronal loss had not been previously documented in these two mutants (Fig. 4D-G and supplemental Fig. 5D,E). To test if VPS35 acts in a cell autonomous manner, we

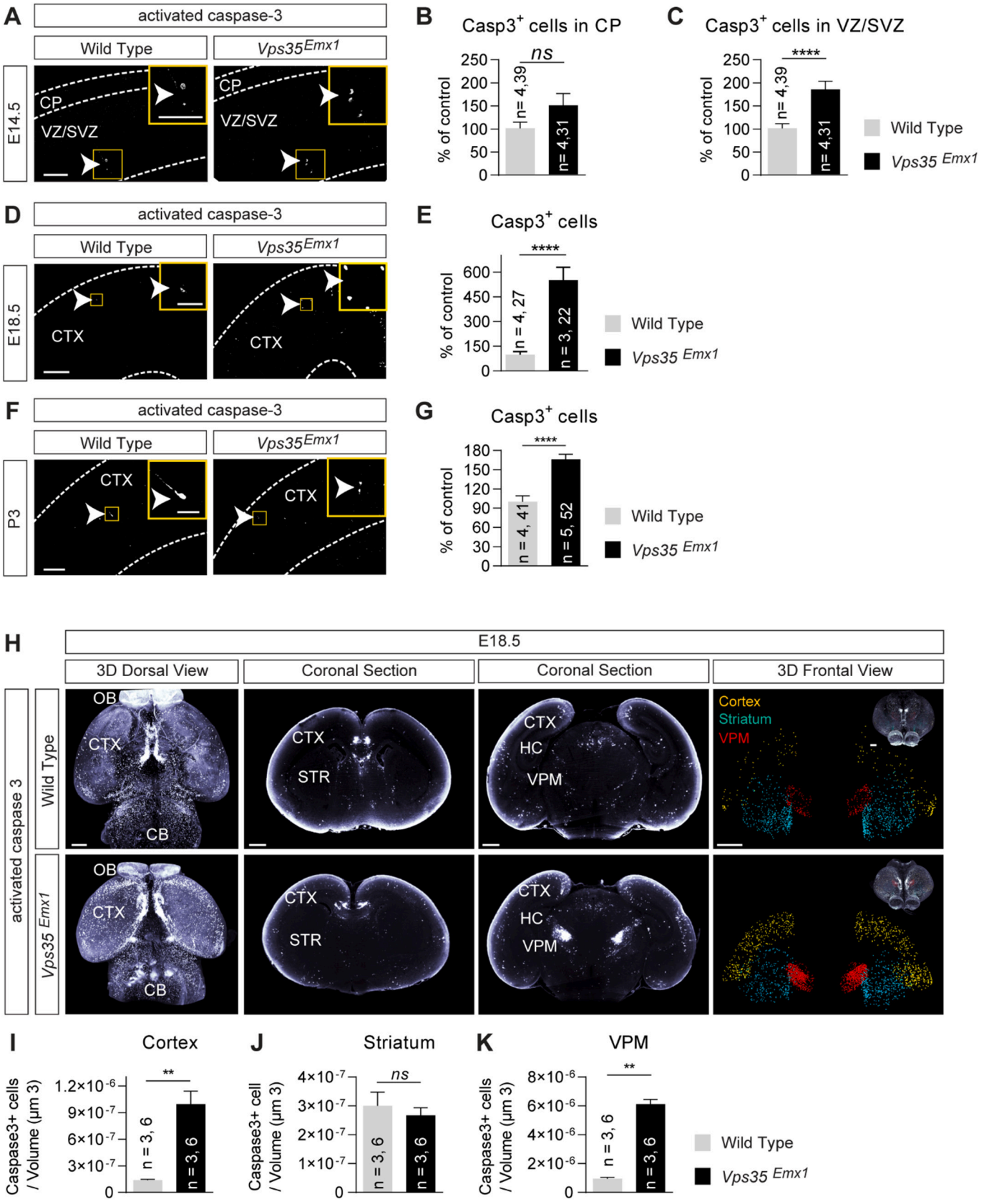

(caption on next page)

Fig. 4. Neurodevelopmental loss of *Vps35*-deficient pyramidal neurons accompanied by a non-autonomous neuronal loss in the thalamus of $Vps35^{Emx1}$ mutants.
A,D,F. Immunostaining of cortical brain sections for activated caspase-3 to mark apoptotic cells of WT and $Vps35^{Emx1}$ cKO animals at indicated ages. Images in yellow boxes are amplified in the upper right panels.
B,C,E,G. Quantification graphs for activated caspase-3 staining. Data represent the mean ± SEM. Mann-Whitney tests.
B. No differences in cell death between cKOs and control animals were noticed in the cortical plate region at E14.5 (n.s. $P = 0.1682$).
C. An 84% increase in cell death at E14.5 in the proliferative region of $Vps35^{Emx1}$ cKO mutants (****$P < 0.0001$).
E, G. Increase in apoptotic cell death is also visible at E18.5, 453% (****P < 0.0001), and P3, 66,2% (***P < 0.0001), respectively.
H. 3D imaging of E18.5 whole brains from WT and $Vps35^{Emx1}$ cKO animals stained for active caspase-3. Immunostaining is presented as a 3D dorsal view in coronal sections, and as in Imaris-based automatic quantification of apoptotic cells.
I-K. Imaris-based automatic quantification graphs for active caspase-3 staining in H for the indicated brain structures. Data represent the mean ± SEM. Mann-Whitney tests.
I. Increase in the total number of apoptotic cells in the entire cerebral cortex [number of caspase-3 positive cells / volume of the neocortex (μm^3) ± S.E.M.: WT, 1.396e-007 ± 1.892e-008 versus cKO, 9.965e-007 ± 3.528e-007 (**$P = 0.0022$).
J. No differences in cell death between cKOs and control animals were observed in the striatum [number of caspase-3 positive cells / volume of the striatum (μm^3) ± S.E.M.: WT, 3.005e-007 ± 1.168e-007 versus cKO, 2.677e-007 ± 6.392e-008 (n.s. $P = 0.5887$)].
K. Massive cell death in the VPM of the thalamus for cKOs when compared to control animals [number of caspase-3 positive cells / volume of the VPM (μm^3) ± S.E.M.: WT, 9.611e-007 ± 2.187e-007 versus cKO, 6.133e-006 ± 7.909e-007 (**P = 0.0022).
CP, cortical plate; SVZ, subventricular zone; VZ, ventricular zone; CTX, cortex; OB, olfactory bulb; CB, cerebellum; STR, striatum; HC, hippocampus; VPM, ventral posterior nucleus. n = x,y where x indicates the number of mice and y the number of sections analyzed for each condition. Scale bars: 50 μm (A and insets in A, D, F), 200 μm (D, F), 500 μm (H, 3D dorsal view; inset on 3D frontal view), 400 μm (H, coronal sections), 300 μm (H, 3D frontal view). (For interpretation of the references to colour in this figure legend, the reader is referred to the web version of this article.)

used in utero electroporation to deliver Cre recombinase plasmids in cortical progenitors of $Vps35^{lox/lox}$ embryos at E14.5 and then analyzed cell death at E17.5. Results showed a clear increase of caspase-3^+ cells in *Vps35* knockout cells compared to control electroporated cells. (supplemental Fig. 6). These results were extended with 3D imaging of E18.5 brain sections stained for active caspase-3, followed by quantification of the total number of apoptotic cells in the entire cerebral cortex (Fig. 4H,I and supplemental Fig. 5F,G). As expected, no difference in cell death was observed in brain regions that were not targeted by *Emx1-Cre* or *Nex-Cre*, such as the striatum (Fig. 4J and supplemental Fig. 5H, L-O). The thalamic region was an exception where massive cell death was observed in the ventral posterior medial (VPM) nucleus (Fig. 4K and supplemental Fig. 5I). This result might explain the decrease in thalamus size as observed previously, although at the prenatal stage (E18.5), the volume of the VPM is not yet reduced (supplemental Fig. 5J,K). Taken together, these results indicate a developmental loss of *Vps35* deficient pyramidal neurons accompanied by non-autonomous neuronal loss in the thalamus.

2.5. Impaired thalamocortical development in Vps35 cKO mutants

To understand how *Vps35* deficiency in the cortex affects the survival of thalamic neurons, we investigated the development of reciprocal projections between the VPM thalamic nucleus and the primary somatosensory cortex (S1). We traced the thalamocortical axons (TCAs) and corticothalamic axons (CTAs) with lipophilic crystal dyes at E14.5, when these projections meet in the internal capsule (Deck et al., 2013). No defects were found in the initial extension and trajectory of TCAs and CTAs in either $Vps35^{Emx1}$ or $Vps35^{Nex}$ cKO embryos (Fig. 5A and supplemental Fig. 7A). In addition, the TCAs correctly reached the mutant S1 cortex at E16.5, as shown in Fig. 5B and S6B. At this stage, TCAs are restricted to the subplate layer in which normal differentiation and distribution of the complexin 3^+ (Cplx3) subplate neurons is observed in both *Vps35* cKOs, although their number is reduced by approximately 36% in both models (supplemental Fig. 8A-D).

At P0, TCAs in WT brains begin to invade the cortical plate and extend radially towards their target Rorβ$^+$ neurons in layer 4 of the developing cortex. In *Vps35* cKO mice, however, the ingrowth of TCAs into the cortical plate was strongly reduced despite the presence and correct positioning of their target cells (Fig. 5C, supplemental Fig. 7C, and supplemental Fig. 8E-J). In contrast, CTAs extending from S1 reach the thalamus and terminate correctly in the VPM and posterior thalamic nuclei (Fig. 5D and supplemental Fig. 7D), showing no impact of *Vps35* deficiency on the establishment of corticothalamic efferent projections. At P3 and P7, the extension and arborization of TCAs in layer 4 was strongly reduced in the thinner cortex of $Vps35^{Emx1}$ and $Vps35^{Nex}$ cKO mice (Fig. 5E-F and supplemental Fig. 7E). Thus, both mutants failed to generate whisker-related barrels in the vibrissal area of S1, as revealed by cytochrome oxidase reactivity or by antibodies against vesicular glutamate-transporter-2 (vGluT2) (Fig. 5G and supplemental Fig. 7F). Whisker-related modules (barreloids) are present in the VPM thalamic nucleus, which show a reduction in size in both *Vps35* cKO mutants (Fig. 5H,I and supplemental Fig. 7G). In contrast, the overall size and barrelette representations in the brainstem trigeminal sensory nucleus were indistinguishable between WT and cKO mice (Fig. 5H,J and supplemental Fig. 7G). Finally, cortical barrels remained undetectable at P21 in both *Vps35* cKO mutants (supplemental Fig. 7H), indicating that barrel formation was not delayed. Taken together, these results suggest that the selective loss of *Vps35* in the developing cerebral cortex makes it a non-permissive environment for the innervation of TCAs. Moreover, the failure to establish proper connections might induce retrograde cell death in the developing thalamus.

2.6. Cortical axon growth and guidance defects in Vps35 cKOs

It has been reported that the initial growth of cortical projections is normal in $Vps35^{Nex}$ cKO mice, but an alteration in axonal terminal differentiation is observed from P14 onwards, concomitant with the onset of neuronal degeneration (Tang et al., 2020). Since earlier onset of neuronal loss is observed in this study (E14.5), we decided to examine the effect of *Vsp35* deletion on the formation of cortical fibre tracts in greater detail. To this end, whole brains from both cKOs at E18.5-P2 were immunostained for PlexinD1 and Neuropilin1 (Nrp1), two axonal receptors for Semaphorin (Sema) guidance molecules that regulate the development of major cortical pathways (Burk et al., 2017; Gu et al., 2003; Mann et al., 2007).

The 3D whole-brain imaging revealed severe hypoplasia of several fibre tracts, including the Nrp1$^+$ hippocampal commissure and corpus callosum (not shown). However, the paths of these commissures did not exhibit any misguidance defects. In particular, the few visible callosal axons extended correctly through the brain midline, and no Probst bundles- indicative of guidance defects in callosal agenesis- were found in $Vps35^{Emx1}$ cKO (not shown).

In contrast, major guidance defects were observed in the PlexinD1$^+$ fibres of the anterior commissure. In $Vps35^{Emx1}$ cKO, ectopic bundles arising from the anterior branch of the anterior commissure extended aberrantly in a caudal direction into the ipsilateral hemisphere (Fig. 6). In addition, some fibres of the stria terminalis failed to enter the anterior commissure to cross to the contralateral side (Fig. 6). These phenotypes are also present in $Vps35^{Nex}$ cKO brains, but with reduced penetrance

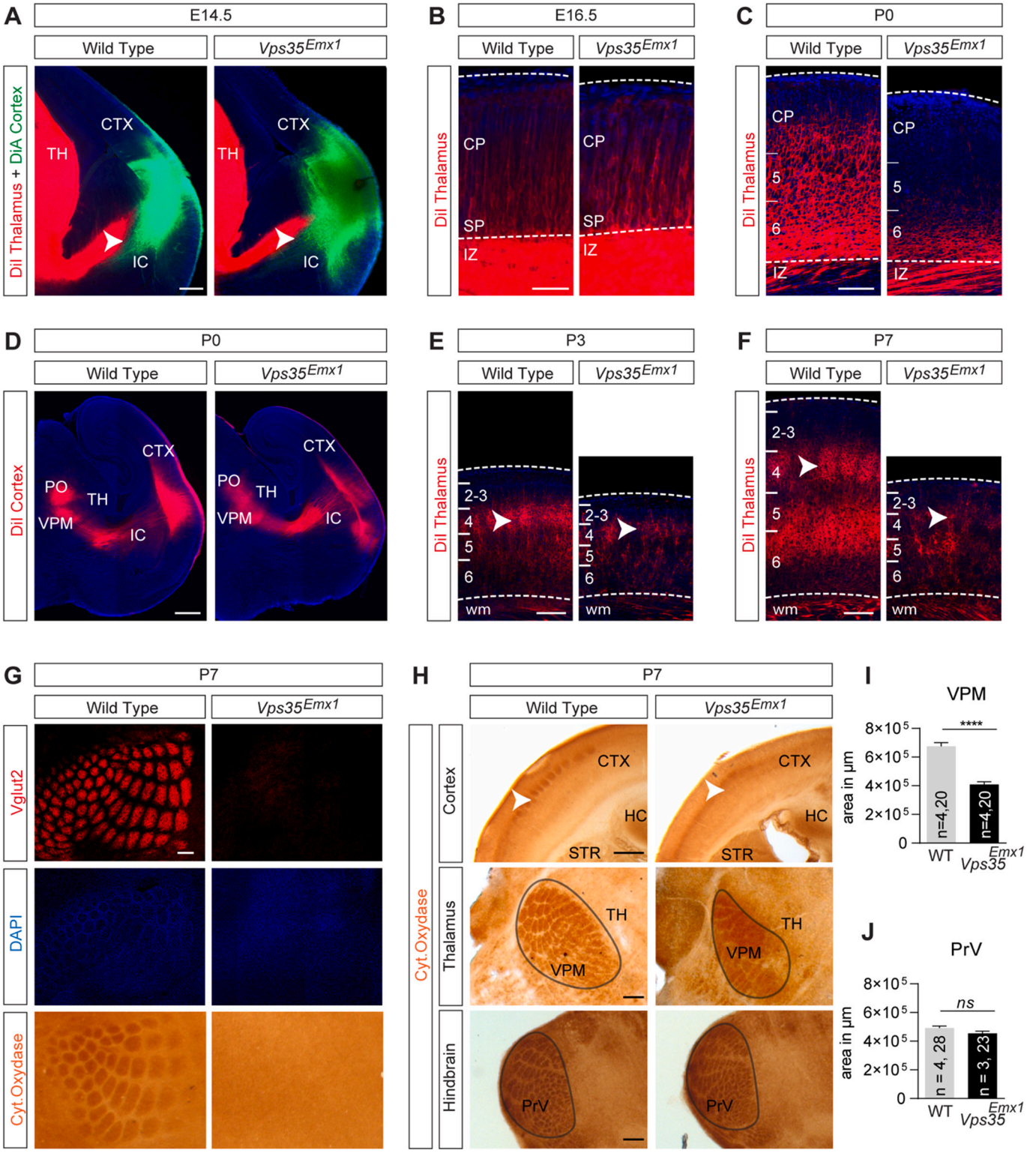

(caption on next page)

Fig. 5. Impaired thalamocortical development in cortex-specific *Vps35*^{Emx1} cKOs. Selective loss of *Vps35* in the developing cerebral cortex leads to the failure in establishing proper connections with TCAs.
A-F. Retrograde labelling of thalamocortical axons (TCAs) after DiI injection in the VPM region of the thalamus, and corticothalamic axons (CTAs) after DiA/DiI injection in the primary somatosensory region (S1) of the cortex of WT and *Vps35*^{Emx1} cKO animals at indicated ages. Cortical areas and layers are indicated.
A. At E14.5, no defect was found in the initial extension and trajectory of TCAs and CTAs (WT, $n = 4/4$ and cKO, $n = 6/6$).
B. TCAs correctly reached the mutant S1 cortex at E16.5 (WT, $n = 5/5$ and cKO, $n = 3/3$).
C. At P0, the ingrowth of TCAs into the cortical plate is strongly reduced, and there are fewer DiI-labelled TCA fibres which extend to the cortical plate, while TCAs in the WT start invading the cortex and extend through the upper layers in the cortical plate (WT, $n = 2/2$ and cKO, $n = 0/3$).
D. At P0, CTAs extending from S1 were directed downward from the cortex through the internal capsule, reaching the thalamus and terminating correctly in the VPM and PO (WT, n = 2/2 and cKO, n = 2/2).
E, F. At P3 and P7, respectively, the extension and arborization of TCAs in layer 4 is strongly reduced in the cortex of *Vps35*^{Emx1} cKO mice (WT, n = 4/4 and cKO, n = 0/4, at P3; WT, n = 2/2 and cKO, n = 0/2, at P7).
G. Immunostaining against vGluT2, DAPI-staining and CO staining (Cytochrome Oxidase) on tangential sections of flattened cortices of WT and *Vps35*^{Emx1} cKO animals at P7. Failure to generate whisker-related barrels in the vibrissal area of S1. Nearly complete loss of TCA inputs, although WT mice had detectable vGluT2-positive and CO-positive S1 areas ($n = 3/3$). There were no barrel-forming fibres in the cortex of *Vps35* mutants or cell-wall clustering of layer 4 neurons around these barrels enclosing TCA patches (n = 3/3).
H. CO staining at P7 of WT and *Vps35*^{Emx1} cKO animals, showing whisker-related modules are present and correctly organised in the brainstem (barrelettes) and a general reduction in the size of the VPM thalamic nucleus (barreloids).
I. Decrease in the area of the VPM (area [μm^2] ± SEM: WT, 676051 ± 25,027 versus cKO, 408,680 ± 19,688 (****$P < 0.0001$).
J. No differences in the area of the PrV between cKOs and control animals [area (μm^2) ± S.E.M.: WT, 49978 ± 13,660 versus cKO, 454,855 ± 15,372 (n.s. $P = 0.0766$).
CTX, cortex; TH, thalamus; IC, internal capsule; CP, cortical plate; SP, subplate; IZ, intermediate zone; VPM, ventral posterior nucleus; PO, posterior thalamic nuclei; wm, white matter; HC, hippocampus; STR, striatum; PrV, principal sensory trigeminal nucleus. n = x,y where x indicates the number of mice and y the number of sections analyzed for each condition. Scale bars: 200 μm (A, E, F, G and H (Thalamus and Hindbrain)), 50 μm (B), 100 μm (C), 500 μm (D, H (cortex)).

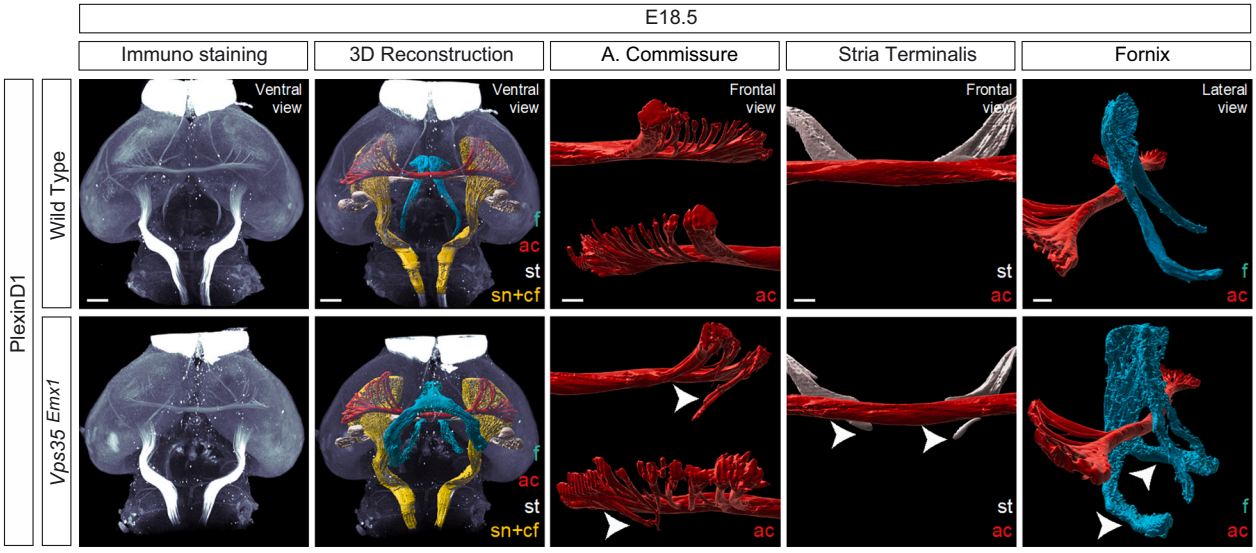

Fig. 6. Cortical axon growth and guidance defects in cortex-specific *Vps35*^{Emx1} cKOs.
Whole brains from E18.5 embryos of WT and *Vps35*^{Emx1} cKO mice were immuno-stained for PlexinD1, followed by 3D reconstructions of light-sheet microscopy images. PlexinD1 labels axons in the post-commissural fornix (pf) (blue), the two branches of the AC, the anterior limb (aac) and the posterior limb (pac) (red), the commissural component of the stria terminalis (st) (white), and the cortico-fugal (cf) plus the striato-nigral (sn) tract projections (yellow) in the mouse brain. 3D whole brain imaging revealed severe hypoplasia of several fibre tracts. Major guidance defects were observed for the PlexinD1$^+$ fibres of the anterior commissure, with ectopic bundles arising from the anterior branch of the ac extending aberrantly in a caudal direction into the ipsilateral hemisphere ($n = 4/4$). In addition, some fibres of the st failed to enter the ac to cross to the contralateral side (n = 4/4). Malformations of the fornix pathway are also evident (n = 4/4). The PlexinD1$^+$ fibres project aberrantly both anteriorly and posteriorly to the ac, and the caudal extension of the pf towards its target is reduced. The cf. projections did not seem to be affected and were without any misrouted fibres. All the observed phenotypes are summarised in Table S1.
Scale bars: 500 μm (Immunostaining, 3D Reconstruction), 200 μm (A. Commissure, Stria Terminalis, Fornix). (For interpretation of the references to colour in this figure legend, the reader is referred to the web version of this article.)

(supplemental Fig. 9). Finally, malformations of the fornix pathway were evident in *Vps35*^{Emx1} cKO mice. The WT fornix displayed pre-commissural (PlexinD1$^-$, Nrp1$^-$) and post-commissural (PlexinD1$^+$, Nrp1$^+$) branches in relation to the anterior commissure (Fig. 6). However, in *Vps35*^{Emx1} cKO, the PlexinD1$^+$ / Nrp1$^+$ fibres project aberrantly both anteriorly and posteriorly to the anterior commissure, and the caudal extension of the post-commissural fornix towards its target, the mammary bodies of the hypothalamus, was reduced (Fig. 6, Table S1). In contrast, fornix development appeared normal in *Vps35*^{Nex} cKO mice (supplemental Fig. 9). The cortico-fugal projections did not seem to be affected in either mutant (Fig. 6 and supplemental Fig. 9). All the observed phenotypes are summarised in Table S1.

Taken together, these results provide evidence that *Vps35* expression in cortical and hippocampal neurons is necessary during embryonic development to direct the initial growth of axonal projections towards their bona fide targets.

3. Discussion

Although dysfunction of the retromer complex is a risk factor for

neurodegenerative disorders, its role in mammalian brain development remains poorly understood. The present results reveal that *Emx1-Cre* and *Nex-Cre* deletion of the *Vps35* retromer component leads to enhanced apoptosis in the embryonic/neonatal cortex and to microcephaly. These results are in contrast to previous studies that showed embryonic deletion of *Vps35* had no impact on early corticogenesis, but induced neuronal apoptosis and progressive cortical atrophy from P14 onwards (Tang et al., 2020; Wu et al., 2020). These discrepancies might be explained by the use of two distinct strains of *Vps35* cKO mice, with loxP sites flanking either exon 4 (this study; de Groot et al., 2013) or exon 6 of *Vps35* (Tang et al., 2020; Wu et al., 2020). If transcripts are produced from the cKO alleles, both would code for the same functional domain of the VPS35 protein (i.e. the sorting nexin-3 interaction domain) and should be degraded, as are most of the alternatively spliced transcript variants of *Vps35* (https://www.ncbi.nlm.nih.gov/ieb/research/acembly/av.cgi?db=mouse&term=vps35&submit=Go). Therefore, differences in phenotypes are most likely due to distinct efficiencies *of Cre recombination,* which can vary according to the genomic position of the loxP sequences and the distance between them in the two *Vps35* cKO lines. A higher gene deletion efficiency could explain the earlier onset of apoptosis observed in the present study.

The precise mechanisms by which loss of retromer function promotes neuronal cell death during development are not yet known. During cortical development, a substantial proportion of neurons are selectively eliminated during a period of cell death, culminating during the first week of postnatal development (Wong and Marín, 2019). This elimination of young postmitotic neurons involves the intrinsic (also referred to as the mitochondrial) apoptotic pathway. Nonetheless, the signals that govern the initial loss of apoptosis repression and/or activation are poorly defined. *Vps35* knockdown has been associated with mitochondrial alterations manifested by a fragmented phenotype, which could contribute to the induction of intrinsic apoptosis in young cortical neurons (Suen et al., 2008; Tang et al., 2015). Recently, it was found that *Vps35* knockdown affects the transport of the anti-apoptotic protein Bcl-xL (extra-large B-cell lymphoma) to the mitochondrial membrane, resulting in an increased apoptosis rate (Farmer et al., 2019). Interestingly, *Bcl-xL;Emx1-Cre* and *Bcl-xL;Nex-Cre* mutant mice show a prenatal onset of enhanced cortical neuron death and a small cortex (Nakamura et al., 2016), a phenotype similar to that observed in $Vps35^{Emx1}$ and $Vps35^{Nex}$ mice.

Our data showed a more severe cortical atrophy in $Vps35^{Emx1}$ mice than in $Vps35^{Nex}$ mice, suggesting an additional function of VPS35 in embryonic neural progenitor cells. Indeed, we found a selective reduction in the number of basal progenitors (also known as intermediate progenitors), which could lead to a lower rate of neurogenesis than in $Vps35^{Nex}$ mice. Cell death is a recently identified mechanism involved in the regulation of basal progenitor cell numbers in vivo (Mihalas and Hevner, 2018). Indeed, a substantial proportion of early basal progenitors divide asymmetrically to generate a basal progenitor and a sister cell that is specified to undergo apoptosis (Mihalas and Hevner, 2018). In the nervous system of the *Drosophila* embryos, such binary cell death is regulated by the unequal partitioning of Numb and inhibition of the pro-apoptotic function of Notch (Orgogozo et al., 2002). Interestingly, the Notch receptor is a cargo protein of the retromer complex, and loss of *Vps35* in *Drosophila* leads to endosomal retention of Notch and ectopic ligand-independent signaling activity (Li et al., 2018). Thus, the question of aberrant Notch activation being responsible for the apoptosis of basal progenitors in the $Vps35^{Emx1}$ cortex is an interesting avenue for further study.

The current study revealed that although *Vps35* is not suppressed in the diencephalon, many molecularly normal thalamic neurons undergo apoptosis at a later stage of gestation. This reduced the thalamic volume in *Vps35* cKO brains. One hypothesis is that such cell death represents an adaptive adjustment mechanism by which the initially normal size of the thalamus is matched to that of the atrophied *Vps35* deficient cortex. Indeed, such a top-down plasticity effect has been observed in the VPM of mice with reduced S1 target area (Eagleson et al., 2007; Zembrzycki et al., 2013). In these animals, competition for cortical space between thalamocortical axons leads to the formation of a miniaturised and incomplete barrel map in S1, while selectively eliminating thalamic neurons that represent the missing body parts (Zembrzycki et al., 2013). However, in *Vps35* cKOs, a clear barrel pattern failed to form in the S1 cortex, suggesting that factors other than a small target size contribute to the observed phenotype.

Tracing experiments have revealed that thalamocortical projections develop normally in embryonic *Vps35* cKO brains but around birth fail to innervate and arborize in S1. At the time of target innervation, thalamic neurons become dependent on cortical-derived trophic signals for their survival (Lotto et al., 2001). One component of this change is the increased expression of brain-derived neurotrophic factor (BDNF) in cortical neurons (Lotto et al., 2001). Thus, the inability to develop an ordered whisker map in the *Vps35* cKO cortex could result from faulty expression of cortical growth and/or trophic factors. In this context, a well-studied cargo of the retromer is the sortilin 1 receptor (Sort1), which binds to and directs numerous ligands, including unprocessed pro-BDNF, to secretion pathways (Kim et al., 2010; Nykjaer and Willnow, 2012). Previous studies have revealed an abnormal lysosomal targeting of Sort1 in *Vps35* deficient cortical neurons (Tang et al., 2020), potentially leading to a decrease in the bioavailability of trophic factors in thalamic neurons. An intriguing and possibly related observation is that apoptosis of thalamic neurons seems to selectively affect the VPM, since little caspase-3 staining was observed in the surrounding thalamic nuclei at E18.5. One explanation might be the higher expression of Trk and p75 neurotrophic receptors in this nucleus (Mooney and Miller, 2007; Tessarollo et al., 1993), thereby rendering these neurons particularly sensitive to modulations by trophic factors.

It has been reported that the retromer plays little role in the early development of axonal projections (Liu et al., 2014; Tang et al., 2020; Wang et al., 2012). Notably, *Vps35*-deficient callosal and hippocampal commissural neurons have been found to normally extend their axons across the brain midline (Tang et al., 2020; Wang et al., 2012). Later, during postnatal maturation and refinement of these projections, *Vps35*-deficient axons begin to show swelling (or spheroids), indicative of axonal damage and degeneration. These have been partly attributed to an alteration in retromer-mediated retrograde transport of BACE1 (β-site amyloid precursor protein (APP) cleaving enzyme 1) (Tang et al., 2020; Wang et al., 2012). This important function of *Vps35* in terminal maturation and maintenance of axonal projections might explain the strong reduction of interhemispheric tracts in adult $Vps35^{Emx1}$ mice.

However, in contrast to these previous studies, the present work revealed that cell-autonomous loss of *Vps35* could cause axons to stall or form aberrant fibre bundles in the prenatal brain, underscoring a previously unknown role of *Vps35* in the growth and guidance of developing axons. Accumulating evidence indicates that endocytic membrane trafficking plays an important role in organising the subcellular distribution of membrane molecules, including receptors for guidance molecules and cell adhesion molecules, to control axon guidance decisions (Pasterkamp and Burk, 2021). Earlier, we had found that the active PlexinD1 receptor, used here as a marker to visualise misguided projections in *Vps35* cKOs, undergoes endocytosis and sorting to recycling endosomes which function as platforms for signal transduction (Burk et al., 2017). Interestingly, a study of the surface proteome of *Vps35* depleted cells has revealed that PlexinD1, among other guidance receptors, is a cargo of the retromer (Steinberg et al., 2013). Since the retromer is involved in the recycling of different membrane receptors, it is possible that the loss of *Vps35* could affect the reinsertion of guidance receptors to the plasma membrane after endocytosis, and thus their ability to be reactivated, as well as access to downstream signaling proteins.

In conclusion, the present results implicate the retromer as a key regulator of corticogenesis and neural circuit formation during embryonic life. As dysfunction of the *Vps35*/retromer is a risk factor for

neurodegenerative diseases, it will be interesting to study carefully whether early neurodevelopmental defects caused by mutations or decreased expression of *Vps35* could predispose the brain to neurodegeneration in later life.

4. Materials and methods

References of the utilised products are provided in the Table S2.

4.1. Generation and maintenance of mice

All animal procedures were conducted in accordance with the guidelines of the European Community (EU Directive 2010/63/EU for animal experiments) and from the French Ministry of Agriculture (agreement number F1305521). Besides, appropriate approval was obtained from the local ethics committee (C2EA-14 agreement 2,015,060,510,102,024-V7 #1186). All mice were housed under standard conditions and maintained at a 12 h dark/light cycle. Hydrated food was provided to the mutant animals from weaning onwards. The background strain of all the mice was C57BL/6. Cortex-specific *Vps35* cKO transgenic mice were generated by crossing $Vps35^{lox/lox}$ mice (de Groot et al., 2013) with *Emx1-Cre* expressing mice (Guo et al., 2000) (referred to as $Vps35^{Emx1}$ cKO), or with *Nex-Cre* expressing mice (Goebbels et al., 2006) (referred to as $Vps35^{Nex}$ cKO). The morning wherein the vaginal plug was observed was considered as embryonic day (E) 0.5, and birth was considered as postnatal day (P) 0. All analyses were performed irrespective of the sex of the animals throughout the study, and for all experiments, littermates were used as controls.

4.2. Tissue preparation and MRI acquisition

For ex vivo MRI acquisitions, skulls containing intact brains were prepared as previously described (Gimenez et al., 2017). Briefly, mice were transcardially perfused with a 4% paraformaldehyde (PFA) solution in phosphate buffered saline (PBS), together with an MRI contrast agent, 6.25 mM gadolinium (Dotarem). The latter is used to improve the visibility of the internal structures and reduce acquisition time. Skulls containing intact brains were dissected and immersed in the same fixing solution for four days, and then transferred to a Fomblin bath for at least seven days to provide a homogeneous distribution of the contrast agent throughout the whole brain (Gimenez et al., 2016). The 3D MRI acquisitions were performed at 9.4 T (Bruker Biospec Avance III). A 3D T1W gradient-echo MRI sequence was used for brain segmentation and volumetric analysis, as previously described (Pagnamenta et al., 2019). Diffusion-weighted images (DWI) were acquired using a 3D spin-echo echo-planar imaging (SE-EPI) sequence with isotropic spatial resolution (80 μm): TE = 17.74 ms; TR = 120 ms, δ = 9 ms, Δ = 13 ms, four signal accumulations, yielding a scan time of approximately 20 h per brain. With these parameters, 16 separate volumes were acquired: 1 T2-weighted volume acquired without diffusion weighting (b = 0 mm^2/s baseline image) and 15 different diffusion-sensitizing gradient directions (b = 2000 s/mm^2). MRI acquisition and reconstruction were performed using Paravision v6.0.1 (Bruker, Ettlingen, Germany).

4.3. Quantitative analysis of brain volumes after MRI acquisitions

Brain regions were defined by MRI segmentation on the 3D T1W MR images. Each cerebral structure was manually segmented using Fiji software and using the Segmentation editor plug-in (http://fiji.sc/Segmentation_Editor) as described (Pagnamenta et al., 2019).

4.4. Tractography after MRI acquisitions

An in-house pipeline based on MRtrix (v3.0_RC3–137, https://www.mrtrix.org/) was used to obtain whole-brain tractograms. After image denoising, unringing, and brain masking, the fibre orientation distributions (FOD; Tournier et al., 2004; Tournier et al., 2007)) were calculated. FODs were generated by performing constrained spherical deconvolution (CSD) and keeping default parameters (for instance, the maximum harmonic order lmax = 4 (Tournier et al., 2013)). Using a probabilistic (Behrens et al., 2003; Parker et al., 2003) streamline tracking approach, whole-brain tractograms were created by seeding every voxel three times. Subsequent to empirical optimisation, the following tracking parameters were applied optimised for the mouse brain: step size = 0.01 mm, radius of curvature = 0.07 mm (Moldrich et al., 2010), min length = 0.1 mm, max length = 50 mm (Aydogan et al., 2018) and cut-off = 0.2, after normalisation of FOD. The major tracts were then isolated from the whole brain tractogram as follows. For each tract, several regions of interest (ROIs) were defined as per the mouse brain atlas (Paxinos and Franklin, 2008). The supplementary Table S3 shows the list of ROIs, with their labels and the orientation in which they were considered, for each tract evaluated in this study.

4.5. Immunolabelling

Fixed brains were sectioned into 50–100-μm thick sections using a Leica Vibratome VT1000S. For flat-mount preparations, cortical hemispheres were dissected and flattened prior to fixation and sectioned tangentially. Immunostaining was performed according to the standard procedures. Tissue sections were incubated in permeabilization buffer (0.3% Triton X-100 in PBS) for 1 h at room temperature (RT), followed by incubation in blocking buffer (0.3% Triton X-100 and 10% donkey serum in PBS) for 1.5 h at RT. Thereafter, the sections were incubated with primary antibodies diluted in blocking buffer overnight at 4 °C, followed by incubation with fluorescent secondary antibodies in permeabilization buffer for 2 h at RT. While using the Rorβ antibody, sections were directly incubated in the blocking buffer overnight at RT after sectioning, and then incubated with the primary antibody diluted in 0.3% Triton X-100 and 1% donkey serum in PBS for three nights at 4 °C, followed by secondary antibodies in 0.3% Triton X-100 and 1% donkey serum in PBS, overnight at RT. All sections were incubated with DAPI (1/2000) in PBS for 20 min at RT to stain the cell nuclei.

4.6. Whole-mount immunostaining and tissue clearing

Whole-mount immunostaining was performed as previously described (Belle et al., 2014), and tissue clearing was done using the iDISCO+ protocol (Renier et al., 2016). Briefly, the brains were dissected and directly fixed by immersion in 4% PFA/PBS for 30 min at RT, followed by 3.5 h at 4 °C. Fixed brains were dehydrated in successive solutions of methanol/PBS and bleached in H_2O_2/methanol overnight at 4 °C. The brains were then rehydrated in methanol/PBS, followed by washes in the blocking solution, PBSGT (0.2% gelatin, 0.1% saponin, 0.5% Triton X-100, and 0.01% Thimerosal in PBS). Thereafter, the brains were incubated for two days in blocking solution at 37 °C. Primary antibodies were diluted in PBSGT and incubated for one week at 37 °C, followed by washes in PBSGT at RT, and secondary antibodies in the same buffer for three days at 37 °C. This was followed by washes in PBSGT at RT. For tissue clearing, brains were dehydrated in methanol/PBS and then delipidated by incubation in dichloromethane (DCM)/methanol for three hours at RT. Finally, the brains were cleared by immersion in dibenzyl ether (DBE) overnight at RT.

4.7. In situ hybridisation

Fixed brains were cryoprotected in two successive baths of 15% sucrose/PBS for 20 min, embedded in Tissue-Tek Optimal Cutting Temperature (OCT) compound at −80 °C, and sectioned at 20 μm in a cryostat (Leica CM3050S). The following RNA probes were used: *Cux1* (Gift from M. Nieto lab), Rorβ (Becker-André et al., 1994), and *Er81* (Arber et al., 2000). Slides were incubated two times in RIPA buffer (150 mM NaCl, 1% NP-40, 0.5% sodium deoxycholate, 0.1% SDS, 1 mM

EDTA, 50 mM Tris-HCL, pH 8.0) for 10 min, then treated for three min with proteinase K (0.008 mg/mL diluted in 50 mM Tris-HCl pH 7.5), and post-fixed for 10 min in 4% PFA/PBS at RT. Sections were treated for 15 min with triethanolamine buffer, equilibrated to a pH of 8 with acetic anhydride, and then washed in 0.1% Tween-20 in PBS. The sections were pre-hybridised for two h at 65 °C with hybridisation buffer (50% formamide, 5× saline-sodium citrate (SSC), 5× Denhardt's solution, 500 μg/mL salmon sperm DNA, and 250 μg/mL yeast RNA). Subsequently, the samples were incubated overnight in a humidified chamber at 65 °C with the probes diluted in the hybridisation buffer at a concentration of 40 μL DNA/mL. The following day, sections were washed twice for one h at 65 °C with the post-hybridisation buffer (50% formamide, 2× SSC, 0.1% Tween-20), and then hybridised and washed, equilibrated in an equilibration buffer B1 (100 mM maleic acid pH 7.5, 150 mM NaCl, 0.1% Tween-20). Thereafter, the sections were blocked in buffer B1 completed with goat serum (10%) for 2 h at RT, and incubated with anti-DIG antibody coupled to alkaline phosphatase, diluted at 1/2000 in the blocking buffer, overnight at 4 °C. After washing with buffer B1, sections were equilibrated in equilibration buffer B2 (100 mM Tris-HCL pH 9.5, 50 mM $MgCl_2$, 100 mM NaCl, 0.1% Tween-20) for 30 min at RT. Colorimetric examination was performed with NBT-BCIP 10× diluted to 1× in buffer B2. The reaction took between two h to one d at RT and was stopped with successive washes with 0.1% Tween-20/PBS. Cryosections were then post-fixed for 15 min in 4% PFA/PBS at room temperature.

4.8. Retrograde labelling with DiI and DiA

Brains were fixed in 4% PFA/PBS overnight at 4 °C and kept in this solution until processing. For E14.5, a small lipophilic crystal dye of DiA (4-(4-dihexadecyl-aminostyryl)-*N*-methyl-pyridinium iodide) was inserted at the surface of the S1 region of the neocortex to label neocortical axons, and then brains were sectioned sagitally to expose the thalamus. The DiI (1,1′-dioctadecyl 3,3,3′,3′-tetramethylindocarbocyanine perchlorate) was injected in the VPM to label thalamic axons. The brains were incubated for 7–10 days in 4% PFA/PBS at 37 °C. E16.5 brains were sectioned sagitally to expose the thalamus, then transversally at the thalamic level to expose the VPM, and DiI crystals were inserted in the VPM to label thalamic axons, followed by two weeks incubation in 4% PFA/PBS at 37 °C. At P0, DiI was inserted into the S1 to label neocortical axons, and for thalamic axons from P0 to P7, brains were sectioned using a vibratome in a caudal to rostral direction to reveal the VPM. DiI was then inserted into the VPM, followed by 5–8 weeks of incubation in 4% PFA/PBS at 37 °C. Brains were cut into 80-μm thick vibratome sections (coronal or 45° sections) and incubated with DAPI for 20 min at RT. The sections were directly imaged to minimise dye diffusion.

4.9. Cytochrome oxidase

After post-fixation, brains were sectioned into 50–100-μm thick sections using a Leica Vibratome. Sections were pre-incubated in 10% sucrose/PBS for 1 h at RT, followed by the revelation solution (10% sucrose, 0.03% cytochrome C, 0.02% catalase, and 0.05% diaminobenzidine (DAB) in PBS) overnight at 37 °C. The following day, the reaction was stopped by washing with PBS.

4.10. Gene expression analysis

E14.5 brains were used to dissect cortex and thalamus from $Vps35^{Emx1}$ cKO or $Vps35^{Nex1}$ cKO, and $Vps35^{lox/lox}$ littermates as controls. Total RNA was extracted using RNeasy micro kit and cDNA was synthetized using SuperScript™ IV First-Strand Synthesis kit following manufacturer's instructions. *Vps35* expression was analyzed by qPCR using StepOnePlus Real-Time PCR Systems and PowerUp™ SYBR™ Green Master Mix. The expression of *Vps35* was normalized against the housekeeping gene beta-actin.

4.11. Imaging acquisition and processing

Data collection and analyses were performed in a blinded manner to genotype when possible, and the conditions of the experiments as well as data collection and processing were performed randomly. Brain sections were imaged using an AxioImager M2 Apotome (Zeiss) equipped with a digital camera (Hamamatsu C11440) or a confocal microscope (Zeiss LSM 780 and LSM 880) for fluorescence. For colorimetric reactions, an AxioImager M2 (Zeiss) equipped with a CamColor camera, or with a Stereoscopic Lumar V12 (Zeiss) was used.

Image processing was performed in Photoshop 2020 for cell counting in 2D sections. To quantify the layer position of the labelled cells, we divided the cortical thickness into 10 bins. In S1, bins 2–3 represent layers 2/3, bin 4–5 represent layer 4, bin 6 represents layer 5a, bin 7 represents layer 5b, and bins 8–10 represent layer 6. For cell number quantification, the number of positive cells in the cortex was counted in a rectangle adapted to the size of the cortex at each stage of development. Caspase-3^+ cells were counted in the entire region corresponding to the structure was analyzed. To determine cortical thickness during development, DAPI sections were measured in the same rostro-caudal region of the S1 area using ImageJ. For each animal, a minimum of three images were quantified (total number of pictures displayed in the graphs for each genotype), and an average was obtained.

3D imaging of cleared brains was performed on a light-sheet fluorescence Ultramicroscope (LaVision BioTec Ultramicroscope II) using the ImspectorPro software. 3D volume images were generated using Imaris software. Volumes were determined based on the autofluorescence of the tissue, created manually with the 'Surface' tool in Imaris. Caspase-3+ cells were counted automatically using the 'Spots' tool in a volume of the neocortex, and for both the striatum and VPM, the caspase-3+ cells were counted in the entire volume of the structure. In each case, counting in the neocortex or cortex was performed at the same rostro-caudal level. Cell counts were normalized to the entire volume of each structure analyzed.

Segmentation of distinct axonal tracts was performed manually using the 'Surface' tool by creating a mask around each volume, followed by 'Surface' performed automatically on the segmentation.

4.12. Statistical analyses

No statistical methods were used to predetermine sample sizes, but our sample sizes were similar to those generally employed in the field. Statistical analyses and graphs were performed using the GraphPad Prism version 8. The data met the assumptions of each statistical test used, so that for each experiment, the normal distribution of the data was examined using the D'Agostino–Pearson omnibus test. n numbers are indicated in the corresponding figures and figure legends. Statistical analyses are performed either on n number of mice, or on n number of sections or ventricles when indicated. The estimate of variance is indicated in the figure graphs and was determined by the SEM of each group. Thus, the results are displayed as mean ± SEM, except for Fig. 1, where the results are displayed as mean ± S.D. The Mann–Whitney test was used to compare the means of two groups of nonparametric data, and the Student's *t*-test and one- or two-way ANOVA followed by the Sidak multiple comparisons test was used to compare differences between more than two groups. Statistical significance was set at $p < 0.05$ (*), $p < 0.01$ (**), $p < 0.001$ (***), and $p < 0.0001$ (****). Statistical details (*p* value, statistical test used) have been included in the figure legends.

CRediT authorship contribution statement

Micaela Roque: Investigation, Writing – original draft. **Diego Alves Rodrigues de Souza:** Investigation. **Martha M. Rangel-Sosa:** Investigation. **Mike Altounian:** Investigation. **Mélanie Hocine:** Investigation.

Jean-Christophe Deloulme: Investigation, Writing – review & editing. **Emmanuel L. Barbier:** Investigation, Writing – review & editing. **Fanny Mann:** Conceptualization, Writing – original draft, Funding acquisition. **Sophie Chauvet:** Conceptualization, Investigation, Writing – original draft, Funding acquisition.

Declaration of competing interest

The authors declare that there are no conflicting interests.

Acknowledgements

We thank the dedicated staff of the IBDM animal house facility and the France-BioImaging infrastructure supported by the Agence Nationale de la Recherche (ANR-10-INSB-04-01, 'Investissements d'Avenir'). We are also grateful to the in vivo experimental platform, the IRMaGE platform and the zootechnicians of the Grenoble Institute Neuroscience (GIN). We thank S. Humbert, GIN, France, and H. C. Korswagen, Hubrecht Institute, Netherlands, for kindly providing the *Nex-Cre* line and *Vps35*$^{lox/lox}$, respectively. We thank N. Chaumontel for performing brain segmentations, E. Denarier for developing macros using Fiji software, and H. Mathieu for help with MRI data acquisition. We thank Sonia Garel and Ludmilla Lokmane, IBENS, France, for their help in performing DiI injections.

Funding

This work was supported by the Centre National de la Recherche Scientifique (CNRS), France; Aix Marseille Université, France; Fondation pour la Recherche Medicale, Equipe FRM DEQ20150331728, France to F.M., Institut Universitaire de France, France, to S.C., Fondation pour la Recherche sur le Cerveau Appel à Projets FRC 2017, France to S.C., M.R. is a recipient of doctoral fellowships from the biotrail Ph.D. Program funded by A*MIDEX, France. This work has received support from the French government under the Programme "Investissements d'Avenir", Initiative d'Excellence d'Aix-Marseille Université via A*Midex funding (AMX-19-IET-004), and ANR (ANR-17-EURE-0029).

Data availability

Raw data from quantification analyses would be available upon request. All other data are available in the main text or supplementary information.

Appendix A. Supplementary data

Supplementary data to this article can be found online at https://doi.org/10.1016/j.mcn.2022.103726.

References

Arber, S., Ladle, D.R., Lin, J.H., Frank, E., Jessell, T.M., 2000. ETS gene Er81 controls the formation of functional connections between group ia sensory afferents and motor neurons. Cell 101, 485–498.

Arnold, S.J., Huang, G.J., Cheung, A.F.P., Era, T., Nishikawa, S.I., Bikoff, E.K., Molnár, Z., Robertson, E.J., Groszer, M., 2008. The T-box transcription factor Eomes/Tbr2 regulates neurogenesis in the cortical subventricular zone. Genes Dev. 22, 2479–2484.

Aydogan, D.B., Jacobs, R., Dulawa, S., Thompson, S.L., Francois, M.C., Toga, A.W., Dong, H., Knowles, J.A., Shi, Y., 2018. When tractography meets tracer injections: a systematic study of trends and variation sources of diffusion-based connectivity. Brain Struct. Funct. 223, 2841–2858.

Barnat, M., Capizzi, M., Aparicio, E., Boluda, S., Wennagel, D., Kacher, R., Kassem, R., Lenoir, S., Agasse, F., Bra, B.Y., et al., 2020. Huntington's disease alters human neurodevelopment. Science 369, 787–793.

Becker-André, M., Wiesenberg, I., Schaeren-Wiemers, N., André, E., Missbach, M., Saurat, J.H., Carlberg, C., 1994. Pineal gland hormone melatonin binds and activates an orphan of the nuclear receptor superfamily. J. Biol. Chem. 269, 28531–28534.

Behrens, T.E.J., Woolrich, M.W., Jenkinson, M., Johansen-Berg, H., Nunes, R.G., Clare, S., Matthews, P.M., Brady, J.M., Smith, S.M., 2003. Characterization and propagation of uncertainty in diffusion-weighted MR imaging. Magn. Reson. Med. 50, 1077–1088.

Belle, M., Godefroy, D., Dominici, C., Heitz-Marchaland, C., Zelina, P., Hellal, F., Bradke, F., Chédotal, A., 2014. A simple method for 3D analysis of immunolabeled axonal tracts in a transparent nervous system. Cell Rep. 9, 1191–1201.

Brodin, L., Shupliakov, O., 2018. Retromer in synaptic function and pathology. Front. Synaptic Neurosci. 10, 1–9.

Burk, K., Mire, E., Bellon, A., Hocine, M., Guillot, J., Moraes, F., Yoshida, Y., Simons, M., Chauvet, S., Mann, F., 2017. Post-endocytic sorting of plexin-D1 controls signal transduction and development of axonal and vascular circuits. Nat. Commun. 8, 14508.

Chen, K.E., Healy, M.D., Collins, B.M., 2019. Towards a molecular understanding of endosomal trafficking by retromer and retriever. Traffic 20, 465–478.

Curtis, M.E., Yu, D., Praticò, D., 2020. Dysregulation of the retromer complex system in down syndrome. Ann. Neurol. 88, 137–147.

Deck, M., Lokmane, L., Chauvet, S., Mailhes, C., Keita, M., Niquille, M., Yoshida, M., Yoshida, Y., Lebrand, C., Mann, F., et al., 2013. Pathfinding of corticothalamic axons relies on a rendezvous with thalamic projections. Neuron 77, 472–484.

Eagleson, K.L., Schlueter McFadyen-Ketchum, L.J., Ahrens, E.T., Mills, P.H., Does, M.D., Nickols, J., Levitt, P., 2007. Disruption of Foxg1 expression by knock-in of cre recombinase: effects on the development of the mouse telencephalon. Neuroscience 148, 385–399.

Farmer, T., O'Neill, K.L., Naslavsky, N., Luo, X., Caplan, S., 2019. Retromer facilitates the localization of bcl-xL to the mitochondrial outer membrane. Mol. Biol. Cell 30, 1138–1146.

Florio, M., Huttner, W.B., 2014. Neural progenitors, neurogenesis and the evolution of the neocortex. Dev. 141, 2182–2194.

Gimenez, U., Perles-Barbacaru, A.T., Millet, A., Appaix, F., El-Atifi, M., Pernet-Gallay, K., van der Sanden, B., Berger, F., Lahrech, H., 2016. Microscopic DTI accurately identifies early glioma cell migration: correlation with multimodal imaging in a new glioma stem cell model. NMR Biomed. 29, 1553–1562.

Gimenez, U., Boulan, B., Mauconduit, F., Taurel, F., Leclercq, M., Denarier, E., Brocard, J., Gory-Fauré, S., Andrieux, A., Lahrech, H., et al., 2017. 3D imaging of the brain morphology and connectivity defects in a model of psychiatric disorders: MAP6-KO mice. Sci. Rep. 7, 10308.

Goebbels, S., Bormuth, I., Bode, U., Hermanson, O., Schwab, M.H., Nave, K.-A., 2006. Genetic targeting of principal neurons in neocortex and hippocampus of NEX-cre mice. Genesis 44, 611–621.

Gotz, M., Stoykova, A., Gruss, P., 1998. Pax6 controls radial glia differentiation in the cerebral cortex. Neuron 21, 1031–1044.

de Groot, R.E.A., Farin, H.F., Macůrková, M., van Es, J.H., Clevers, H.C., Korswagen, H. C., 2013. Retromer dependent recycling of the wnt secretion factor wls is dispensable for stem cell maintenance in the mammalian intestinal epithelium. PLoS One 8, 1–9.

Gu, C., Rodriguez, E.R., Reimert, D.V., Shu, T., Fritzsch, B., Richards, L.J., Kolodkin, A.L., Ginty, D.D., 2003. Neuropilin-1 conveys semaphorin and VEGF signaling during neural and cardiovascular development. Dev. Cell 5, 45–57.

Guo, H., Hong, S., Jin, X.L., Chen, R.S., Avasthi, P.P., Tu, Y.Te, Ivanco, T.L., Li, Y., 2000. Specificity and efficiency of cre-mediated recombination in Emx1-cre knock-in mice. Biochem. Biophys. Res. Commun. 273, 661–665.

Kim, E., Lee, Y., Lee, H.J., Kim, J.S., Song, B.S., Huh, J.W., Lee, S.R., Kim, S.U., Kim, S.H., Hong, Y., et al., 2010. Implication of mouse Vps26b-Vps29-Vps35 retromer complex in sortilin trafficking. Biochem. Biophys. Res. Commun. 403, 167–171.

Li, B., Wong, C., Gao, S.M., Zhang, R., Sun, R., Li, Y., Song, Y., 2018. The retromer complex safeguards against neural progenitor-derived tumorigenesis by regulating notch receptor trafficking. elife 7, 1–28.

Liu, W., Tang, F.L., Erion, J., Xiao, H., Ye, J., Xiong, W.C., 2014. Vps35 haploinsufficiency results in degenerative-like deficit in mouse retinal ganglion neurons and impairment of optic nerve injury-induced gliosis. Mol. Brain 7, 1–11.

Lotto, R.B., Asavaritikrai, P., Vali, L., Price, D.J., 2001. Target-derived neurotrophic factors regulate the death of developing forebrain neurons after a change in their trophic requirements. J. Neurosci. 21, 3904–3910.

Mann, F., Chauvet, S., Rougon, G., 2007. Semaphorins in development and adult brain: implication for neurological diseases. Prog. Neurobiol. 82, 57–79.

Mihalas, A.B., Hevner, R.F., 2018. Clonal analysis reveals laminar fate multipotency and daughter cell apoptosis of mouse cortical intermediate progenitors. Development 145, dev164335.

Moldrich, R.X., Pannek, K., Hoch, R., Rubenstein, J.L., Kurniawan, N.D., Richards, L.J., 2010. Comparative mouse brain tractography of diffusion magnetic resonance imaging. NeuroImage 51, 1027–1036.

Mooney, S.M., Miller, M.W., 2007. Nerve growth factor neuroprotection of ethanol-induced neuronal death in rat cerebral cortex is age dependent. Neuroscience 149, 372–381.

Nakamura, A., Swahari, V., Plestant, C., Smith, I., McCoy, E., Smith, S., Moy, S.S., Anton, E.S., Deshmukh, M., 2016. Bcl-xL is essential for the survival and function of differentiated neurons in the cortex that control complex behaviors. J. Neurosci. 36, 5448–5461.

Nykjaer, A., Willnow, T.E., 2012. Sortilin: a receptor to regulate neuronal viability and function. Trends Neurosci. 35, 261–270.

Orgogozo, V., Schweisguth, F., Bellaïche, Y., 2002. Binary cell death decision regulated by unequal partitioning of numb at mitosis. Development 129, 4677–4684.

Pagnamenta, A.T., Heemeryck, P., Martin, H.C., Bosc, C., Peris, L., Uszynski, I., Gory-Fauré, S., Couly, S., Deshpande, C., Siddiqui, A., et al., 2019. Defective tubulin detyrosination causes structural brain abnormalities with cognitive deficiency in humans and mice. Hum. Mol. Genet. 28, 3391.

Parker, G.J.M., Haroon, H.A., Wheeler-Kingshott, C.A.M., 2003. A framework for a streamline-based probabilistic index of connectivity (PICo) using a structural

interpretation of MRI diffusion measurements. J. Magn. Reson. Imaging 18, 242–254.
Pasterkamp, R.J., Burk, K., 2021. Axon guidance receptors: endocytosis, trafficking and downstream signaling from endosomes. Prog. Neurobiol. 198, 101916.
Paxinos, G., Franklin, K.B.J., 2008. Paxinos and Franklin's the Mouse Brain in Stereotaxic Coordinates, Third Edit. Elsevier.
Pocha, S.M., Wassmer, T., Niehage, C., Hoflack, B., Knust, E., 2011. Retromer controls epithelial cell polarity by trafficking the apical determinant crumbs. Curr. Biol. 21, 1111–1117.
Prasad, B.C., Clark, S.G., 2006. Wnt signaling establishes anteroposterior neuronal polarity and requires retromer in C. Elegans. Development 133, 1757–1766.
Renier, N., Adams, E.L., Kirst, C., Wu, Z., Azevedo, R., Kohl, J., Autry, A.E., Kadiri, L., Venkataraju, K.U., Wang, V.X., et al., 2016. Mapping of brain activity by automated volume analysis of immediate early genes. Cell 165, 1789–1802.
Seaman, M.N.J., 2012. The retromer complex-endosomal protein recycling and beyond. J. Cell Sci. 125, 4693–4702.
Small, S.A., Kent, K., Pierce, A., Leung, C., Kang, M.S., Okada, H., Honig, L., Vonsattel, J. P., Kim, T.W., 2005. Model-guided microarray implicates the retromer complex in Alzheimer's disease. Ann. Neurol. 58, 909–919.
Steinberg, F., Gallon, M., Winfield, M., Thomas, E.C., Bell, A.J., Heesom, K.J., Tavaré, J. M., Cullen, P.J., 2013. A global analysis of SNX27-retromer assembly and cargo specificity reveals a function in glucose and metal ion transport. Nat. Cell Biol. 15, 461–471.
Strutt, H., Langton, P.F., Pearson, N., McMillan, K.J., Strutt, D., Cullen, P.J., 2019. Retromer controls planar polarity protein levels and asymmetric localization at intercellular junctions. Curr. Biol. 29, 484–491.
Suen, D.-F., Norris, K.L., Youle, R.J., 2008. Mitochondrial dynamics and apoptosis. Genes Dev. 22, 1577–1590.
Tang, F., Liu, W., Hu, J., Erion, J.R., Ye, J., Mei, L., Xiong, C., Hospital, D., Military, T., 2015. VPS35 deficiency or mutation causes dopaminergic neuronal loss by impairing mitochondrial fusion and function. Cell Rep. 12, 1631–1643.
Tang, F.L., Zhao, L., Zhao, Y., Sun, D., Zhu, X.J., Mei, L., Xiong, W.C., 2020. Coupling of terminal differentiation deficit with neurodegenerative pathology in Vps35-deficient pyramidal neurons. Cell Death Differ. 27, 2099–2116.
Tessarollo, L., Tsoulfas, P., Martin-Zanca, D., Gilbert, D.J., Jenkins, N.A., Copeland, N.G., Parada, L.F., 1993. TrkC, a receptor for neurotrophin-3, is widely expressed in the developing nervous system and in non-neuronal tissues. Development 118, 463–475.
Tournier, J.D., Calamante, F., Gadian, D.G., Connelly, A., 2004. Direct estimation of the fiber orientation density function from diffusion-weighted MRI data using spherical deconvolution. NeuroImage 23, 1176–1185.
Tournier, J.D., Calamante, F., Connelly, A., 2007. Robust determination of the fibre orientation distribution in diffusion MRI: non-negativity constrained super-resolved spherical deconvolution. NeuroImage 35, 1459–1472.
Tournier, J.D., Calamante, F., Connelly, A., 2013. Determination of the appropriate b value and number of gradient directions for high-angular-resolution diffusion-weighted imaging. NMR Biomed. 26, 1775–1786.
Vilariño-Güell, C., Wider, C., Ross, O.A., Dachsel, J.C., Kachergus, J.M., Lincoln, S.J., Soto-Ortolaza, A.I., Cobb, S.A., Wilhoite, G.J., Bacon, J.A., et al., 2011. VPS35 mutations in parkinson disease. Am. J. Hum. Genet. 89, 162–167.
Wang, C.L., Tang, F.L., Peng, Y., Shen, C.Y., Mei, L., Xiong, W.C., 2012. VPS35 regulates developing mouse hippocampal neuronal morphogenesis by promoting retrograde trafficking of BACE1. Biol. Open 1, 1248–1257.
Wen, L., Tang, F.L., Hong, Y., Luo, S.W., Wang, C.L., He, W., Shen, C., Jung, J.U., Xiong, F., Lee, D.Hoon, et al., 2011. VPS35 haploinsufficiency increases Alzheimer's disease neuropathology. J. Cell Biol. 195, 765–779.
Wong, F.K., Marín, O., 2019. Developmental cell death in the cerebral cortex. Annu. Rev. Cell Dev. Biol. 35, 523–542.
Wu, K.Y., Tang, F.L., Lee, D., Zhao, Y., Song, H., Zhu, X.J., Mei, L., Xiong, W.C., 2020. Ependymal Vps35 promotes ependymal cell differentiation and survival, suppresses microglial activation, and prevents neonatal hydrocephalus. J. Neurosci. 40, 3862–3879.
Zembrzycki, A., Chou, S.J., Ashery-Padan, R., Stoykova, A., O'Leary, D.D.M., 2013. Sensory cortex limits cortical maps and drives top-down plasticity in thalamocortical circuits. Nat. Neurosci. 16, 1060–1067.
Zhou, B., Wu, Y., Lin, X., 2011. Retromer regulates apical-basal polarity through recycling crumbs. Dev. Biol. 360, 87–95.
Zimprich, A., Benet-Pagès, A., Struhal, W., Graf, E., Eck, S.H., Offman, M.N., Haubenberger, D., Spielberger, S., Schulte, E.C., Lichtner, P., et al., 2011. A mutation in VPS35, encoding a subunit of the retromer complex, causes late-onset parkinson disease. Am. J. Hum. Genet. 89, 168–175.